

Cite this: *Analyst*, 2019, **144**, 412Received 31st October 2018,
Accepted 29th November 2018
DOI: 10.1039/c8an02099j

rsc.li/analyst

A facile synthesis of perforated reduced graphene oxide for high performance electrochemical sensors†

Hong Wei,^a Dawei Pan,^b  ^{*b,c} Su Ma,^a Guangheng Gao^d and Dazhong Shen  ^{*a}

Highly active perforated reduced graphene oxide (P-rGO) was synthesized by a facile methodology based on co-deposition of graphene oxide with sacrificial Prussian blue. Electrode surface properties were characterized by SEM and EDS. The GC/P-rGO electrode exhibited a larger specific surface area than that of GCE. These findings highlighted that the signal was enhanced for both dopamine detection and selenium detection by using P-rGO as a relevant supporting substrate. The result indicated that the large number of perforated structures formed numerous electrically conductive channels in the structure, improving the electro-catalytic properties.

Graphene is a typical two-dimensional carbon network that has attracted sustained attention in many fields, including both theoretical electrochemistry and applied electrochemistry.¹ However, the two-dimensional structure of graphene restricts the expansion of its surface area. The 3D perforated graphene nanostructures integrate the intrinsic properties of pristine graphene with peculiar characteristics like high thermal conductivity, large specific surface area, and unique catalytic properties.

Various methods have been used for the preparation of 3D graphene. Examples include chemical vapor deposition,² template processing,³ self-assembly,⁴ and hydrothermal

reduction.⁵ Template processing is particularly intriguing due to the ease of operation and relatively low power consumption. The method could be divided into two categories: hard and soft templates. Hard templates like nickel foam⁶ and aluminum-based template⁷ require cumbersome steps to remove the template, which are time-consuming.

By comparison, soft templates are relatively more simple and convenient. They were firstly reported by Qian *et al.*,³ who fabricated 3D graphene chitosan composites by freezing them in liquid nitrogen and studied their electrochemical properties. Li *et al.*⁸ prepared a 3D-rGO film in a liquid phase by adding GO sheets, ethanol-amine, and copper hydroxide nano-strands. However, these methods require harsh conditions and post-treatment to deal with the organic solution. Hence, mild, facile and inexpensive routes are highly desirable for the fabrication of 3D graphene.

Prussian blue (PB) is easily available⁹ and can be synthesized by chemical¹⁰ or electrochemical deposition.^{11,12} Predominantly, the electro-synthesis strategies of PB attracted increasing attention due to easy handling and an efficient synthesis path. The distinct characteristics of PB and high susceptibility to alkaline media provide great potential for practical application in nanomaterial design and template application.¹³ To the best of our knowledge, no reports are so far published on the preparation of three-dimensional graphene using PB as the template. Herein, a mild route was employed to synthesize three-dimensional perforated reduced graphene oxide.

The stepwise assembly process of a P-rGO modified electrode is illustrated in Scheme 1 and the details are described in the ESI.† Firstly, a GO–PB mixture was electro-polymerized on the electrode by cyclic voltammetry. Then the electrode surface was subsequently treated by continuous cleaning with 0.5 M NaOH and 0.1 M H₂SO₄ solutions for five minutes to easily remove PB. Fig. 1 illustrates a typical process of the electropolymerization of the rGO@PB film. In the first cycle, the peak at –1.3 V was assigned to the irreversible reduction of GO, which then vanished during the second cycle.¹⁴ The

^aCollege of Chemistry, Chemical Engineering and Materials Science, Collaborative Innovation Center of Functionalized Probes for Chemical Imaging in Universities of Shandong, Key Laboratory of Molecular and Nano Probes, Ministry of Education, Shandong Provincial Key Laboratory of Clean Production of Fine Chemicals, Shandong Normal University, Jinan 250014, P.R. China.

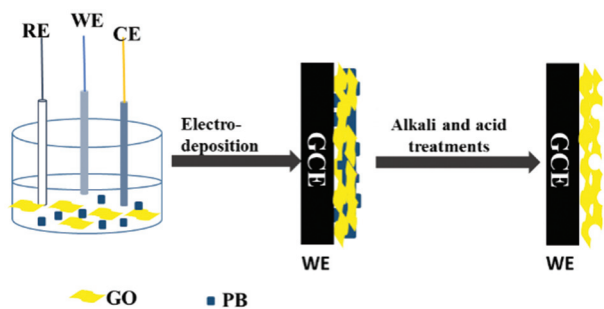
E-mail: dzshen@sdsu.edu.cn; Tel: +86 531 86180740

^bKey Laboratory of Coastal Environmental Processes and Ecological Remediation, Yantai Institute of Coastal Zone Research, Chinese Academy of Sciences, Yantai 264003, P.R. China. E-mail: dwpan@yic.ac.cn; Fax: +86 535 2109155; Tel: +86 535 2109155

^cUniversity of Chinese Academy of Sciences, Beijing 100049, P.R. China

^dBiology Institute, Qilu University of Technology (Shandong Academy of Sciences), Key Laboratory for Biosensors of Shandong Province, Jinan 250353, P.R. China

†Electronic supplementary information (ESI) available. See DOI: 10.1039/c8an02099j



Scheme 1 The schematic illustration of the stepwise assembly procedure.

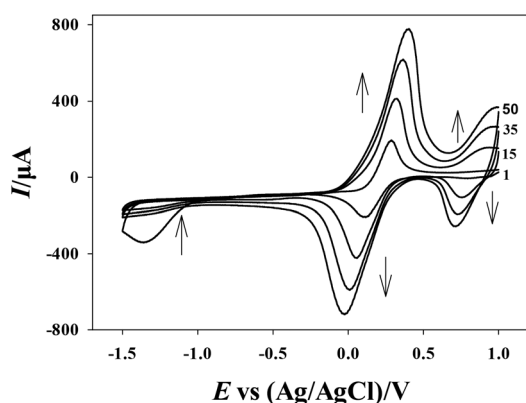
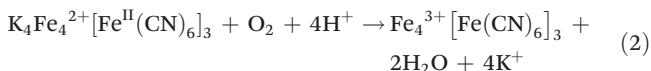


Fig. 1 Electropolymerization of the PB and rGO film by continuous cycling in 30 mM $\text{K}_3\text{Fe}(\text{CN})_6$ + 30 mM FeSO_4 + 0.5 mg mL^{-1} rGO aqueous solution at a scan rate of 0.2 V s^{-1} . Numerals indicate the number of cycles and arrows show the trend of peak current shift.

contact between GO and the electrode surface would induce an electrochemical reduction to produce insoluble rGO. This should slightly adhere to the electrode surface.

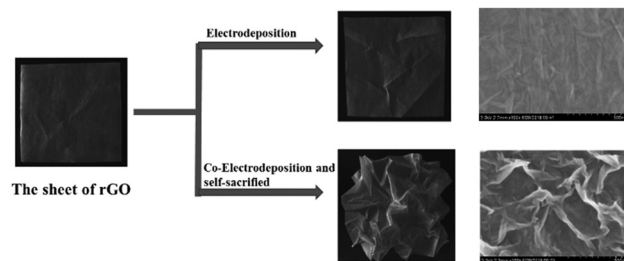
The mechanism of electrodeposition reactions of PB could be summarized by two fundamental steps. The redox peak between 0.6 V–1.0 V was due to low spin $\text{Fe}(\text{CN})_6^{3-/4-}$, while that from -0.2 V–0.6 V was attributed to low spin $\text{Fe}^{3+/2+}$.¹⁵ As the scanning number increased, all redox peaks gradually grew and then tended to stabilize, indicating the formation of a PB film on the substrate surface. These processes are explained by eqn (1) and (2):¹⁶



The electro-polymerization data demonstrated that rGO and PB were effectively combined on the electrode surface.

Scanning electron microscopy (SEM) was employed to characterize the morphologies of rGO, rGO@PB, and 3D P-rGO nanomaterials. The SEM images of P-rGO/AuNDs are shown in the ESI (Fig. S1†). As can be seen, the AuNDs exhibited a nano-dendritic structure on the electrode. SEM and energy disper-

sive X-ray spectroscopy (EDS) strongly confirmed the successful electropolymerization of the PB and rGO film, as well as the complete etching of the PB template (ESI†). Paper models were utilized to illustrate the SEM response (Scheme 2). The morphologies of rGO with the slight wrinkled flat sheets were clearly presented on planar contours (Fig. 2a and b). In Fig. 2c and d, PB particles were evenly embedded in the interior and surface of rGO, preventing rGO from aggregation. As shown in



Scheme 2 A paper model was utilized to illustrate the synthesis process of the slightly wrinkled 2D rGO and the perforated 3D rGO.

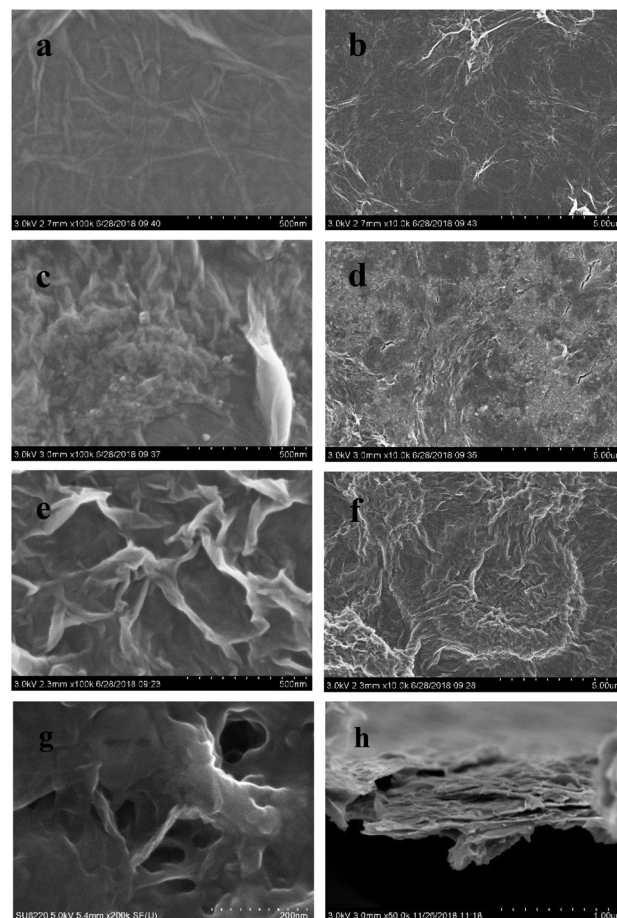


Fig. 2 SEM images of GC/rGO (a, b), GC/rGO@PB (c, d) and GC/P-rGO (e, f). High magnification (g) and cross-sectional SEM (h) images of GC/P-rGO.

Fig. 2e and f, the surface morphology of P-rGO exhibited more heavily crumpled open structures. After the removal of PB by alkali and acid treatments, the P-rGO surface became hierarchical forming layer upon layer of peaks and knolls. The high magnification and cross-sectional SEM images of GC/P-rGO are shown in Fig. 2g and h. P-rGO possesses a number of porous structures with a pore size of 100–200 nm and the P-rGO film thickness is approximately 1 μm . Different electrochemical deposition cycles result in different thicknesses of the deposited films. The thickness of P-rGO varies with the number of deposition cycles. Overall, PB played a vital role in converting 2D sheets into heavily perforated three-dimensional structures.

To evaluate the electrochemical reactivity of modified electrodes, cyclic voltammetry (CV) and electrochemical impedance spectroscopy (EIS)¹⁷ were carried out in 5 mM $\text{K}_3\text{Fe}(\text{CN})_6$ and $\text{K}_4\text{Fe}(\text{CN})_6$ containing 0.1 M KCl as the supporting electrolyte. As shown in Fig. 3A, the presence of P-rGO or rGO could increase the peak current of the redox probe when compared to a single bare electrode. The GC/P-rGO electrode exhibited enhanced response compared to GC/rGO. The result indicated the advantages of the larger specific surface area and higher conductivity of GC/P-rGO.

To gain a further insight into the electrode kinetics about surface change, EIS was used at the different electrodes. As shown in Fig. 3B, the electron transfer resistance (R_{et} , equal to a semicircle diameter of EIS) of GCE, GC/rGO and GC/P-rGO was calculated to be 143 Ω , 83 Ω and 52 Ω , respectively. The Nyquist plot of the P-rGO electrode exhibited the lowest R_{ct} compared to that of GCE, indicating the excellent interface properties of GC/P-rGO. In general, the proposed synthetic method was efficient.

The catalytic performances of the P-rGO electrode were investigated as a support substrate. The linear sweep voltammetry (LSV) tests were performed in 0.1 mol L^{-1} phosphate buffer solution (pH 7.0) containing different concentrations of dopamine (DA) and the data are presented in Fig. 4. At a DA concentration of 1 $\mu\text{mol L}^{-1}$ (bottom of Fig. 4A), the anodic peak currents of GC, GC/rGO and GC/P-rGO were recorded as 0.072 μA , 0.34 μA and 1.12 μA , respectively. Hence, the peak current value of the P-rGO electrode was 3.5-fold higher than

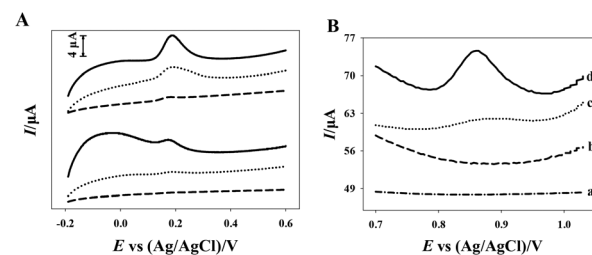
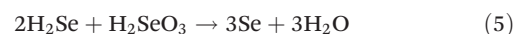
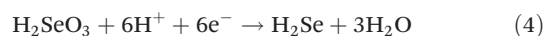
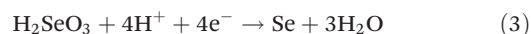


Fig. 4 A: SWV of bare GCE (dashed curve), GC/rGO (dotted curve) and GC/P-rGO (solid curve) in 0.1 M PBS (pH 7.0) containing 1 μM DA (bottom of the figure) or 10 μM DA (top of the figure). B: SWV of bare GCE (a), GC/rGO (b), GC/rGO/AuNPs (c) and GC/P-rGO/AuNPs (d) in 0.1 M PBS (pH 7.0) containing 100 nM $\text{Se}(\text{IV})$.

that of rGO and 15.5-fold superior to that of the bare electrode. At a DA concentration of 10 $\mu\text{mol L}^{-1}$ (top of Fig. 4A), the anodic peak current of GC, GC/rGO and GC/P-rGO was estimated to be 0.47 μA , 2.19 μA and 4.62 μA , respectively. Thus, the peak current value of the P-rGO electrode was 2.1-fold higher than that of rGO and 10-fold superior to that of the bare electrode. The presence of P-rGO with the perforated structure increases the electron transport capability. Meanwhile, the increased active area of P-rGO collectively promotes the increase of the response current 15 times higher than that of the bare electrode for dopamine oxidation. In Fig. 4A, compared with the rGO modified electrode and the bare electrode, the peak potential of the P-rGO modified electrode was shifted to the negative potential, and the peak shape was sharper. The result illustrated that the presence of the P-rGO material makes DA more susceptible to oxidation. The peak potentials of the calibration graphs of three electrodes toward successive additions of DA ranging from 0.8 to 15 μM are shown in Fig. S3.† Compared with other electrodes, the P-rGO modified electrode revealed higher efficiency and higher sensitivity. As expected, P-rGO possessed ultrahigh catalytic performances due to the elevated surface areas of perforated graphene.

To explore the feasibility of 3D graphene in the conductive channels of the anchored materials, sensors were assembled and tested. Sensitive and selective sensors based on P-rGO supported gold nanodendrites (AuNDs) were specifically prepared according to the procedure of Segura *et al.*¹⁸ AuNDs/P-rGO/GCE platforms were used to determine $\text{Se}(\text{IV})$ by anodic stripping voltammetry in 1 mmol L^{-1} HClO_4 according to Fig. 4B and the details are compiled in the ESI.† In acidic media, the mechanism of electroactive $\text{Se}(\text{IV})$ reduction changed with the potential. The involved processes are proposed in eqn (3)–(5):^{19–21}



The reduction in eqn (3) may take place at positive potentials. At negative potentials, eqn (4) will first occur. H_2Se

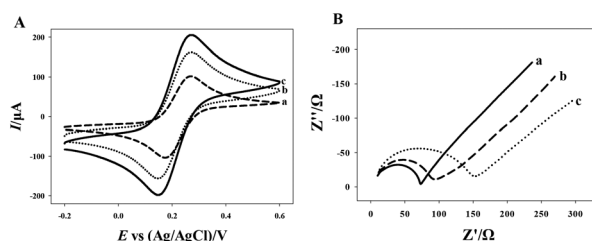


Fig. 3 A: CVs of bare GCE (a), GCE/rGO (b) and GCE/P-rGO (c) in the potential range of -0.2 V to 0.6 V. Scan rate: 0.1 V s^{-1} . B: Impedance spectra (Nyquist plots) of GC/P-rGO (a), GC/rGO (b) and bare GCE (c). The data are recorded in the presence of 5 mM $\text{K}_3\text{Fe}(\text{CN})_6$ and $\text{K}_4\text{Fe}(\text{CN})_6$ as a redox label.

species were not stable in solution and swiftly react with H_2SeO_3 to form elemental selenium, according to eqn (5). The reduction of Se(IV) can be described by the transformation of Se(IV) into Se(0) though this may utilize different mechanisms on the electrode surface.

Fig. 4B shows the compared oxidation currents of Se(IV) at different electrodes. The anodic peak currents of Se(IV) at GC and GC/rGO looked not obvious. The anodic peak currents of Se(IV) at GC/P-rGO/AuNDs was recorded as $7.47\ \mu\text{A}$, which was 7.5-fold higher than that of GC/rGO/AuNDs ($0.99\ \mu\text{A}$). Hence, the GC/P-rGO/AuNDs electrode was suitable for the determination of Se(IV) due to its high conductivity and large surface area. Ultimately, the advantages of P-rGO nanomaterials with elevated electrochemical activities were verified in terms of both detection and catalysis.

In summary, a facile route based on one-step co-electrodeposition of GO and PB mixture and the self-sacrificed of PB, was employed to fabricate perforated rGO. PB was utilized as a “clean” template with high efficiency and versatile bright characteristics. The proposed route should be versatile for the electrodeposition of various three-dimensional nanomaterials. The facile synthesis route of the proposed method and its wide applications would be useful in the electrocatalysis and electrochemistry of three-dimensional nanomaterial structures.

Conflicts of interest

There are no conflicts to declare.

Acknowledgements

This work was financially supported by the National Natural Science Foundation of China (21575080), the Youth Innovation Promotion Association (2011170) and the Equipment Development Project (YZ201558) of the Chinese Academy of Sciences.

Notes and references

- 1 D. A. C. Brownson, D. K. Kampouris and C. E. Banks, *Chem. Soc. Rev.*, 2012, **41**, 6944.
- 2 Z. P. Chen, W. C. Ren, L. B. Gao, B. L. Liu, S. F. Pei and H. M. Cheng, *Nat. Mater.*, 2011, **10**, 424.
- 3 L. Qian and L. Lu, *RSC Adv.*, 2014, **4**, 38273.
- 4 B. Tang, Z. Y. Xiong, X. W. Yun and X. G. Wang, *Nanoscale*, 2018, **10**, 4113.
- 5 Q. X. Xie, Y. F. Zhang and P. Zhao, *Mater. Lett.*, 2018, **225**, 93.
- 6 G. J. Hu, C. Xu, Z. H. Sun, S. G. Wang, H. M. Cheng, F. Li and W. C. Ren, *Adv. Mater.*, 2016, **28**, 1603.
- 7 P. Nautiyal, M. Mujawar, B. Boesl and A. Agarwal, *Carbon*, 2018, **137**, 502.
- 8 J. C. Li, C. H. Weng, F. C. Tsai, W. P. Shih and P. Z. Chang, *Appl. Phys. Lett.*, 2016, **108**, 013108.
- 9 C. L. Lin and L. C. Liao, *Surf. Coat. Technol.*, 2014, **259**, 330.
- 10 S. Demiri, M. Najdoski and J. Velevska, *Mater. Res. Bull.*, 2011, **46**, 2484.
- 11 J. W. Zhao, Y. Zhang, C. G. Shi, H. Y. Chen, L. M. Tong, T. Zhu and Z. F. Liu, *Thin Solid Films*, 2006, **515**, 1847.
- 12 R. Yang, Z. B. Qian and J. Q. Deng, *J. Electrochem. Soc.*, 1998, **145**, 2231.
- 13 L. Chao, X. J. Xiong, J. Liu, A. G. Xu, T. Huang, F. He and Q. J. Xie, *Sens. Actuators, B*, 2017, **253**, 603.
- 14 Y. Y. Jiang, Y. Z. Lu, F. H. Li, T. S. Wu, L. Niu and W. Chen, *Electrochem. Commun.*, 2012, **19**, 21.
- 15 D. W. Pan, J. H. Chen, L. H. Nie, W. Y. Tao and S. Z. Yao, *Electrochim. Acta*, 2004, **49**, 795.
- 16 K. Itaya, N. Shoji and I. Uchida, *J. Am. Chem. Soc.*, 1984, **106**, 3423.
- 17 Q. Hong, L. M. Yang, Z. H. Liu and F. Li, *Analyst*, 2018, **143**, 3327.
- 18 R. Segura, J. Pizarro, K. Diaz, A. Placecio, F. Godoy, E. Pino and F. Recio, *Sens. Actuators, B*, 2015, **220**, 263.
- 19 V. Beni, G. Collins and D. W. Arrigan, *Anal. Chim. Acta*, 2011, **699**, 127.
- 20 A. Manzoli, M. C. Santos and S. A. S. Machado, *Thin Solid Films*, 2007, **515**, 6860.
- 21 S. K. Maria, *J. Electroanal. Chem.*, 1983, **148**, 233.